Delft University of Technology

Regime transitions in near-surface temperature inversions

A conceptual model

Van de Wiel, Bas J.H.; Vignon, Etienne; Baas, Peter; van Hooijdonk, Ivo G.S.; van der Linden, Steven J.A.; van Hooft, J. Antoon; Bosveld, Fred C.; de Roode, Stefan R.; Moene, Arnold F.; Genthon, Christophe

DOI
10.1175/JAS-D-16-0180.1

Publication date
2017

Document Version
Final published version

Published in
Journal of the Atmospheric Sciences

Citation (APA)
Van de Wiel, B. J. H., Vignon, E., Baas, P., van Hooijdonk, I. G. S., van der Linden, S. J. A., van Hooft, J. A., Bosveld, F. C., de Roode, S. R., Moene, A. F., & Genthon, C. (2017). Regime transitions in near-surface temperature inversions: A conceptual model. *Journal of the Atmospheric Sciences*, *74*(4), 1057-1073. https://doi.org/10.1175/JAS-D-16-0180.1

Important note
To cite this publication, please use the final published version (if applicable).
Please check the document version above.

Copyright
Other than for strictly personal use, it is not permitted to download, forward or distribute the text or part of it, without the consent of the author(s) and/or copyright holder(s), unless the work is under an open content license such as Creative Commons.

Takedown policy
Please contact us and provide details if you believe this document breaches copyrights.
We will remove access to the work immediately and investigate your claim.

This work is downloaded from Delft University of Technology.
For technical reasons the number of authors shown on this cover page is limited to a maximum of 10.

Regime Transitions in Near-Surface Temperature Inversions: A Conceptual Model

BAS J. H. VAN DE WIEL,[a] ETIENNE VIGNON,[b,c] PETER BAAS,[a] IVO G. S. VAN HOOIJDONK,[d] STEVEN J. A. VAN DER LINDEN,[a] J. ANTOON VAN HOOFT,[a] FRED C. BOSVELD,[e] STEFAN R. DE ROODE,[a] ARNOLD F. MOENE,[f] AND CHRISTOPHE GENTHON[c,b]

[a] *Faculty of Civil Engineering and Geosciences, Department of Geoscience and Remote Sensing, Delft University of Technology, Delft, Netherlands*
[b] *CNRS/Université Grenoble Alpes, Laboratoire de Glaciologie et Géophysique de l'Environnement, Grenoble, France*
[c] *CNRS, Laboratoire de Glaciologie et Géophysique de l'Environnement, Grenoble, France*
[d] *Fluid Dynamics Laboratory, and J.M. Burgerscentrum, Eindhoven University of Technology, Eindhoven, Netherlands*
[e] *Royal Netherlands Weather Institute, De Bilt, Netherlands*
[f] *Wageningen University and Research Centre, Wageningen, Netherlands*

(Manuscript received 10 June 2016, in final form 23 December 2016)

ABSTRACT

A conceptual model is used in combination with observational analysis to understand regime transitions of near-surface temperature inversions at night as well as in Arctic conditions. The model combines a surface energy budget with a bulk parameterization for turbulent heat transport. Energy fluxes or feedbacks due to soil and radiative heat transfer are accounted for by a "lumped parameter closure," which represents the "coupling strength" of the system.

Observations from Cabauw, Netherlands, and Dome C, Antarctica, are analyzed. As expected, inversions are weak for strong winds, whereas large inversions are found under weak-wind conditions. However, a sharp transition is found between those regimes, as it occurs within a narrow wind range. This results in a typical S-shaped dependency. The conceptual model explains why this characteristic must be a robust feature. Differences between the Cabauw and Dome C cases are explained from differences in coupling strength (being weaker in the Antarctic). For comparison, a realistic column model is run. As findings are similar to the simple model and the observational analysis, it suggests generality of the results.

Theoretical analysis reveals that, in the transition zone near the critical wind speed, the response time of the system to perturbations becomes large. As resilience to perturbations becomes weaker, it may explain why, within this wind regime, an increase of scatter is found. Finally, the so-called heat flux duality paradox is analyzed. It is explained why numerical simulations with prescribed surface fluxes show a dynamical response different from more realistic surface-coupled systems.

1. Introduction

In this work a simple conceptual model is introduced to understand and predict regime transitions of near-surface temperature inversions in the nocturnal and polar atmospheric boundary layer. Observational studies as well as results from numerical simulations indicate that clear-sky nocturnal and polar boundary layers experience a qualitative change with respect to both turbulent characteristics and near-surface stability, when the wind becomes weak. This regime shift is known as the transition from the weakly stable boundary layer (WSBL) to the very stable boundary layer (VSBL; Mahrt et al. 1998; Poulos et al. 2002; Zilitinkevich et al. 2008; Fernando and Weil 2010; Sun et al. 2012; Acevedo et al. 2016).

The present work departs at recent work by the authors. In Van de Wiel et al. (2012a,b, hereafter VdW12a,b) it was shown that the aforementioned regime transition can be understood in terms of the so-called maximum sustainable heat flux theory (MSHF). This paper provides a comprehensive framework in which the merits and open ends

Denotes content that is immediately available upon publication as open access.

Corresponding author e-mail: Bas J. H. Van de Wiel, b.j.h.vandewiel@tudelft.nl

DOI: 10.1175/JAS-D-16-0180.1

© 2017 American Meteorological Society. For information regarding reuse of this content and general copyright information, consult the AMS Copyright Policy (www.ametsoc.org/PUBSReuseLicenses).

of that work may be understood. The MSHF theory can be summarized as follows: In stably stratified flow, the amount of heat that can be transported downward by the (turbulent) flow is limited to a maximum. As the turbulent heat flux is limited for weak and very strong stratification, the maximum occurs at moderate stability. Under clear-sky conditions, the longwave radiative heat loss at the surface may become significantly larger than the maximum, particularly under weak-wind conditions. A large imbalance in the surface energy budget results, which enhances stability. The turbulent heat flux decreases further, which then causes a larger imbalance (positive feedback). Finally, as a result of the intense stratification, turbulent activity becomes very weak and the VSBL sets in.

The magnitude of the sensible heat flux maximum strongly depends on the ambient wind speed. It is this sensitivity, which causes the transition toward the VSBL to be sharply defined in terms of wind speed. In VdW12b an expression for this threshold, coined ''minimum wind speed for sustainable turbulence,'' was given. Van Hooijdonk et al. (2015, hereafter VH15) applied the framework to a large climatological dataset from Cabauw, Netherlands. By comparing the ambient wind to its threshold value, the transition between the VSBL and the WSBL was predicted in agreement with observations. Interestingly, the same dataset was analyzed by Monahan et al. (2015). Although they followed a different route, using hidden Markov models, they arrived at similar conclusions regarding the classification of the data in terms of the maximum sustainable heat flux.

The viewpoint of the MSHF was used by Donda et al. (2015) in order to understand regime transitions in direct numerical simulations of flux-driven stably stratified channel flows. In Nieuwstadt (2005) and Flores and Riley (2011) a sudden transition of turbulent to nonturbulent flow was reported in cases when the surface heat extraction exceeds a certain limit. Donda et al. (2015) showed that the transition can be understood in terms of the MSHF theory and that the critical point can be predicted in terms of external forcing parameters.

In spite of these promising aspects, a shortcoming of the MSHF theory is that it assumes the ''heat flux demand'' at the surface is known in advance. In a numerical simulation this is the case when a prescribed flux is imposed as a lower boundary condition. In atmospheric practice, however, this is obviously not the case: the sensible heat flux is an integral part of the full surface energy budget. Its value will therefore vary depending on the circumstances and characteristics of the underlying surface (Holtslag et al. 2007). Therefore, in order to apply the MSHF concept in its traditional form, one has to make practical assumptions. One could, for example, assume that, in order to prevent rapid surface cooling, the turbulent heat flux should be able to bring up at least a significant fraction of the net radiative heat loss. This was done by Van Hooijdonk et al. (2015), who assumed that at least 10 W m^{-2} should be supported by the flow in order to prevent rapid surface cooling under clear-sky conditions. This value is then used to calculate the wind speed threshold. Although the computed threshold is robust and not very sensitive to the exact value of this input parameter, the assumption itself clearly introduces an empirical factor, which limits universality of the results.

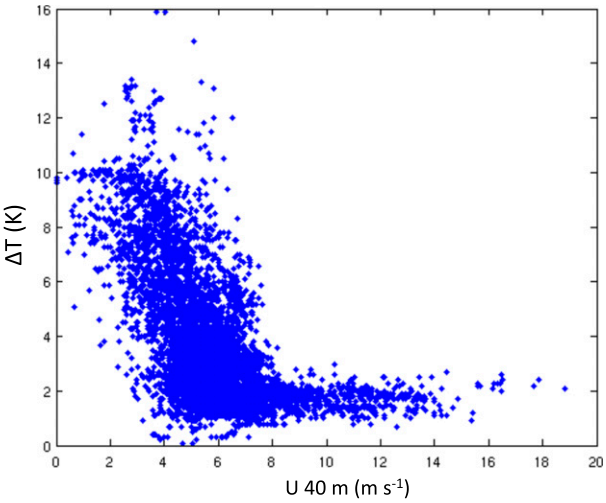

FIG. 1. Temperature inversion between 40 and 0.1 m, as a function of wind speed at 40 m as observed at Cabauw for the period Aug 2013–Dec 2015 (clear skies only, between 0000 and 0300 UTC; see section 2).

The second limitation of the theory is connected to this. In a flux-driven system, the threshold wind speed marks the point where the positive feedback takes over and near-surface stability rapidly intensifies. However, no statements are made what happens when the wind speed is lower than its threshold value. It is expected that negative feedback processes such as soil heat transport and reduced emission of longwave surface radiation will impact on near-surface stability. They will eventually offset the initial positive feedback, so that even in case with no turbulence, a new thermodynamic equilibrium will emerge (Duynkerke 1999; Steeneveld et al. 2006; Edwards 2009; Acevedo et al. 2012; Bosveld et al. 2014b). As shown below, here we will tackle the limitations addressed above and generalize MSHF theory by explicitly accounting for surface feedbacks.

As an illustration of the scope of this paper, an observational example is given in Fig. 1. It depicts how the strength of the temperature inversion between 40 and 0.1 m, depending on the magnitude of the wind

at the 40-m level at Cabauw. Data between 0000 and 0300 UTC are shown as to represent reasonably stationary conditions (for more details refer to section 2).

A typical "S shaped" dependence is observed: For strong winds the dependence of the inversion on wind speed is rather weak. When the wind speed becomes less than a certain threshold ($\sim$6–7 m s^{-1}), the inversion strength sharply increases until, for very low speeds, it levels off to $\sim$10 K. Note that not only the mean inversion itself but also its variability appears to be a function of wind speed: observational scatter in the wind speed range of 8–15 m s^{-1} appears to be much smaller than, for example, in the range 2–6 m s^{-1}.

Study of near-surface inversions is of societal importance—for example, in order to predict whether local frost events may occur. In spring, for example, unexpected ground frost will be detrimental in agricultural practice when freezing of fruit tree blossom causes significant yield losses. Likewise, a frost event may affect human safety when roads become slippery. Reliable forecasts are therefore essential in order to take timely and adequate road management measures. Strong temperature inversions also promote the occurrence of fog events (Roman-Cascon et al. 2016), which impact on traffic safety through reduced visibility. In aviation, this will translate in reduced flight activity, which causes significant economic losses (Stolaki et al. 2012). Finally, transitions in near-surface temperature inversions are also of importance for climate studies. As global climate models often have poor resolution, sharp transitions such as in Fig. 1 are largely smoothened out. As explained by McNider et al. (2012) and Walters et al. (2007) this may (partly) explain the poor performance in matching diurnal temperature range tendencies seen in observations. This interesting aspect will be addressed in section 3.

As earlier work focused on the threshold wind speed only, no predictions were made about what happens below this point: what if the wind speed becomes less than its critical value? In terms of Fig. 1, only the right-hand part for winds greater than 7 m s^{-1} was concerned. Here, we will consider the full wind range. An extension of the MSHF theory is presented in the form of a simple conceptual model, which adds rudimentary feedbacks by surface radiation and soil heat transport. Emphasis lies in understanding of those feedbacks rather than in model complexity. As such, the negative feedbacks by radiation and soil are combined in a single, "lumped" parameter. The term lumped is borrowed from the field of hydrology where a single, effective parameter, such as the average water storage capacity, may be used to characterize a complex hydrological catchment as a whole (Beven 2001). Also in our system the lumped parameter is a semiempirical, site-dependent one. Therefore the outcome of the model can be no more than indicative of complex reality. On the other hand, it will be shown that major characteristic dependencies, such as depicted in Fig. 1, can be explained and that a remarkably close resemblance to observations is obtained. The model can therefore serve as a benchmark for studies with more complex and more realistic models of the SBL. To contrast the results found for Cabauw, as representative of a moderate climate, also observational results for Dome C, Antarctica, will be presented. It will be shown that the differences between the sites can be explained by the differences in the strength of surface feedbacks.

As the first part of this study focuses on surface inversions in their equilibrium state, in the second part also the resilience of the equilibrium to perturbations (in a sense of dynamic instability) is studied theoretically. We investigate how an equilibrium system will respond to natural fluctuations. Boundary layer turbulence is essentially a stochastic process such that spontaneous excursion from equilibrium will occur frequently. It will be explained that under those conditions strongly coupled systems behave qualitatively different from systems that have weak or no coupling, with respect to their dynamical stability. In a general sense, it will be shown that the resilience of the system to perturbation becomes much weaker when the wind speed drops under its critical value. Amongst other effects, this may partly explain the wind speed dependence of observational scatter, such as observed in Fig. 1.

The work is organized as follows. In section 2 the conceptual bulk model is introduced. Equilibrium solutions for different values of the lumped parameter are presented in section 3, where also observational data from Dome C are presented. An operational model (in column mode) is run in order to assess the generality of the results obtained by the conceptual model.

In section 4 the physical mechanism behind the regime transition is investigated and it is shown that the maximum sustainable heat flux principle also applies to the new surface-coupled model. In section 5 an expression for the threshold wind speed is derived. Theoretical perturbation analysis and its practical implications for coupled and noncoupled systems are discussed in section 6. Finally, conclusions are summarized in section 7.

2. Model description

In this section a brief model description is given. For an in-depth discussion on assumptions, refer to VdW12b, where similar formulations are used in a different context. We combine a surface energy budget with a bulk

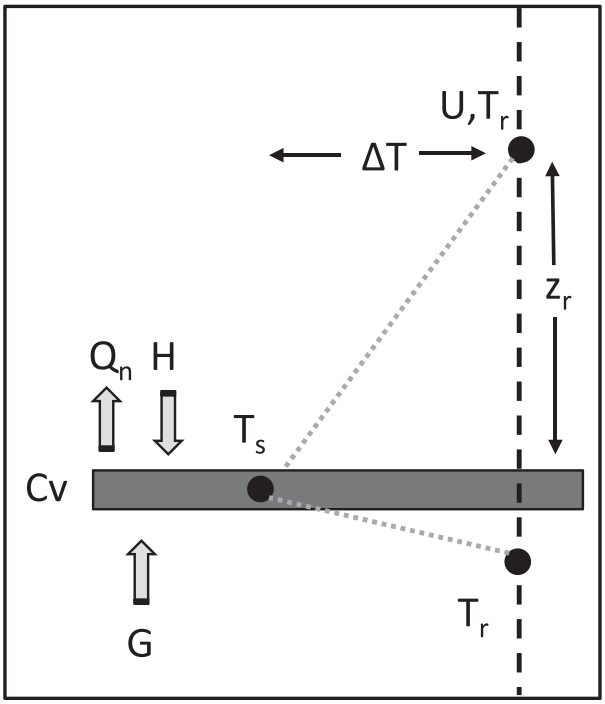

FIG. 2. Schematic view of the bulk model. Black dots refer to temperatures at the surface (dynamic) and in the atmosphere and soil (fixed references). Inversion strength is indicated by ΔT.

model of the lower atmosphere. The resulting equation describes the evolution of the near-surface inversion strength. A schematic view is given in Fig. 2. We take the so-called velocity crossing height as a reference level z_r. This can be explained as follows. At night, winds at higher levels usually tend to accelerate by an inertial oscillation as a result of flow decoupling (Blackadar 1957). Near the surface, winds weaken owing to a combination of inertial effects and turbulent stress divergence around sunset (Thorpe and Guymer 1977; Baas et al. 2012). At intermediate heights (some decameters above the surface), a "crossing level" exists where the wind remains relatively constant in magnitude. At Cabauw, wind speeds are relatively constant at levels between 40 and 60 m above the ground [a climatology is provided in VH15 and in Wieringa (1989)]. In the following we assume the wind speed to be constant during the night at z_r. Though this assumption is rather crude, extension to more realistic dynamical forcing could be made in future model versions.

As temperature tendencies at this height are typically much smaller than surface temperature tendencies, we also assume temperature at reference height T_r to be constant, though it is realized that in reality T_r will also depend on the evolution of the NBL as a whole. The inversion strength between the reference r and the surface s is defined as $\Delta T = T_r - T_s$. To simplify, we assume that T_r is also representative for the temperature in the topsoil, so that the bulk temperature difference between the surface and soil is represented by ΔT as well. As discussed below this is an oversimplification of reality, where generally the topsoil temperature will differ from T_r. Alternatively, more general models could be constructed using, for example, $T_g = \beta T_r$, with T_g the topsoil temperature and β a site-specific parameter (J. C. Wyngaard 2016, personal communication). To avoid additional parameter estimation, we opt for simplest alternative here. In any case, it is expected that the difference between the topsoil and the surface will be most sensitive to the value surface temperature itself as its daily cycle has the largest amplitude. Below, it will be shown that the model is able to reproduce typical temperature inversion characteristics that are found in observations and that the results are similar to those obtained with a realistic column model.

The evolution equation for the inversion strength ΔT is governed by the surface energy balance:

$$C_v \frac{d\Delta T}{dt} = Q_n - G - H, \tag{1}$$

where C_v is the heat capacity of the surface (e.g., vegetation, snow) per unit area ($\mathrm{J\,m^{-2}\,K^{-1}}$). The net longwave radiative flux is denoted by Q_n, the sensible heat flux by H, and the soil heat flux by G ($\mathrm{J\,m^{-2}\,s^{-1}}$). For mathematical convenience positive signs are given to all fluxes: the loss term Q_n (directed outward) as well as the gain terms H and G (directed toward the surface). In this way all numbers in Eq. (1) are positive by definition (note that alternative conventions are also possible; e.g., Wyngaard 2010).

As motivated below, the fluxes are parameterized, which leads to our model equation:

$$C_v \frac{d\Delta T}{dt} = Q_i - \lambda \Delta T - \rho c_p c_D U \Delta T f(R_b), \tag{2}$$

where Q_i is the so-called isothermal net radiation (explained below) and λ is the lumped parameter ($\mathrm{J\,m^{-2}\,s^{-1}\,K^{-1}}$), which represents feedbacks from both soil heat conduction and radiative cooling (see below). Symbols ρ and c_p represent the density ($\mathrm{kg\,m^{-3}}$) and heat capacity of air at constant pressure ($\mathrm{J\,kg^{-1}\,K^{-1}}$). The neutral drag coefficient is denoted by $c_D = [\kappa/\ln(z_r/z_0)]^2$, with $\kappa \approx 0.4$ the von Kármán constant and z_0 the roughness length (assumed equal for momentum and heat). The wind speed at reference height z_r is given by U. Finally, the stability function $f(R_b)$ depends on bulk Richardson number: $R_b \equiv z_r(g/T_r)(\Delta T/U^2)$.

In the net radiative budget both surface and atmosphere are modeled as gray bodies with effective emissivities.

From Boltzmann's law the net loss of energy at the surface becomes

$$Q_n = \varepsilon_s \sigma T_s^4 - \varepsilon_r \sigma T_r^4, \tag{3}$$

with $\sigma = 5.67 \times 10^{-8}\,\mathrm{W\,m^{-2}\,K^{-4}}$, surface emissivity ε_s, and air emissivity ε_r. Strictly speaking, the amount of longwave radiation absorbed by the surface should be multiplied by the emissivity of the surface (Kirchhoff's law). As most natural surfaces have an emissivity close to 1, this effect is ignored in the present study for reasons of simplicity. We linearize the second term around T_r:

$$\begin{aligned} Q_n &= (\varepsilon_s - \varepsilon_r)\sigma T_r^4 - 4\varepsilon_s \sigma T_r^4 (T_r - T_s) \\ &= Q_i - \lambda_{\mathrm{rad}} \Delta T, \end{aligned} \tag{4}$$

with $\lambda_{\mathrm{rad}} = 4\sigma\varepsilon_s T_r^3$. By definition, the isothermal net radiation Q_i equals the net radiation in case the atmosphere is isothermal (Monteith 1981; Holtslag and De Bruin 1988). The advantage of this concept is that one separates radiative loss due to external factors (difference in atmosphere and surface emissivity) from the part that depends on internal variables (surface temperature/inversion). The radiative "exchange coefficient" λ_{rad} indicates how fast the magnitude of Q_n decreases with increasing inversion strength. For example, using $\varepsilon_s = 1$ and $T_r = 285\,\mathrm{K}$, we find $\lambda_{\mathrm{rad}} \approx 5\,\mathrm{W\,m^{-2}\,K^{-1}}$.

Next, the negative feedback in radiation is combined with a similar feedback coming from soil heat transport. Formally, the latter is a complex process, which depends on the full temperature history in the soil itself (Heusinkveld et al. 2004). In line with the discussion above, we crudely parameterize by adopting a simple linear relation: $G = \lambda_s \Delta T$. The idea is that stronger inversions will favor more transport of heat from the soil. Values of λ_s over isolating surfaces like grass will typically be lower than their bare soil counterparts. Even lower values are expected over fresh snow. To indicate the order of magnitude, Steeneveld et al. (2006) found $\lambda_s \approx 5\,\mathrm{W\,m^{-2}\,K^{-1}}$ over prairie grass. Both feedbacks are combined by defining the lumped conductance: $\lambda = \lambda_{\mathrm{rad}} + \lambda_s$. It is site-specific and has to be obtained from fitting the model to observations. As it has a strongly empirical character, the discussions above must be seen as physical arguments for the order of magnitude, rather than as a precise process description.

Turbulent heat transport is described in terms of bulk properties using Monin–Obukhov similarity in its integrated form: $H = \rho c_p c_D U \Delta T f(Rb)$ (Louis 1979). Different forms of the stability function will be investigated, as to represent functions that are encountered typically in the atmospheric literature. Of course, similar analysis could be performed with any stability function. In Fig. 3 three characteristic expressions are visualized:

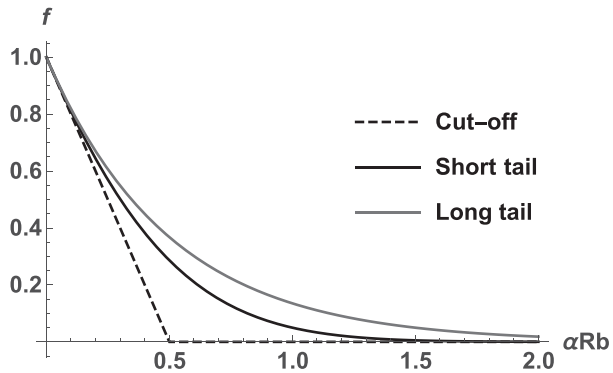

FIG. 3. Stability functions used to model turbulent heat exchange (see text).

- the cutoff function: $\begin{matrix} f(R_b) = (1 - 2\alpha R_b), & R_b \le 1/\alpha \\ f(R_b) = 0, & R_b > 1/\alpha \end{matrix}$,
- the short-tail function: $f(R_b) = \exp[-2\alpha R_b - (\alpha R_b)^2]$, and
- the long-tail function: $f(R_b) = \exp(-2\alpha R_b)$.

Coefficient α is empirical. In accordance with observations of Högström (1996), we take $\alpha = 5$. At weak stability the functions are similar. The cutoff function is less realistic from an observational perspective, but it facilitates mathematical analysis in the second part of this work. The short-tail function is close to $f(R_b) = (1 - \alpha R_b)^2$, which is consistent with log-linear similarity functions that are representative of atmospheric observations (England and McNider 1995; Högström 1996). In operational weather forecast models sometimes "long tail" stability functions with enhanced mixing (as compared to observationally based functions) are used in order to describe turbulent exchange. The practical motivation for this choice is often large-scale model performance (Holtslag et al. 2013; Louis 1979). To assess the effect of enhanced mixing on the inversion strength, also a long-tail stability function is introduced here.

3. Equilibrium solutions

a. Results from the conceptual model

In this section we study equilibrium solutions of Eq. (2). Default input values are given in Table 1, which are taken to represent climatology at Cabauw and Dome C, Antarctica (VH15; Genthon et al. 2010, 2013; Vignon et al. 2017a,b). As the emphasis lies on conceptual understanding, numbers should be considered as indicative. A detailed, one-to-one comparison with observations is beyond the scope of this work. To estimate the lumped parameter λ, the following procedure

TABLE 1. Parameter values used for conceptual modeling. Cabauw values are used in Fig. 4. Idem for Fig. 5, but with variable λ values. Values representing Dome C are used in Fig. 6b.

	z_0 (m)	z_r (m)	Q_i (W m^{-2})	λ (W m^{-2} K^{-1})	T_r (K)	P (hPa)	ρ (kg m^{-3})	c_p (J kg^{-3} K^{-1})
Cabauw	0.03	40	70	7	285	1013	1.2	1005
Dome C	$10^{-2}/10^{-4}$	10	50	2	243	645	1.0	1005

was followed. First, a value for Q_i of 70 is assumed for clear-sky conditions at Cabauw, following Holtslag and De Bruin (1988). The value of Q_i can be estimated from Q_n data as its limiting value under conditions of very strong winds and clear skies (i.e., nearly isothermal conditions). Next, we reconsider Fig. 1 and observe that a maximum inversion strength ΔT of about 10 K occurs when the wind speed vanishes. Now λ can be estimated using the equilibrium solution of Eq. (2) in the limit of zero wind speed: $\lambda = Q_i/\Delta T$. As such, we find $\lambda = 70/10 = 7\,\mathrm{W\,m^{-2}\,K^{-1}}$. A similar procedure was followed to estimate the lumped parameter for Dome C (Fig. 6).

In Fig. 4 the equilibrium solution for ΔT is given as a function of wind speed at reference height using the Cabauw values of Table 1. Three different stability functions are represented. For the non-cutoff functions, Fig. 4 looks remarkably similar to the observational example of Fig. 1: a typical S-shape dependence is found. From right to left, the inversion only gradually increases with decreasing wind. Then, within a small wind speed window, the inversion strength suddenly increases, until it levels off again. At the same time it is noted that the leveling off in the left-hand side of the graph is more pronounced in the model predictions than in the observations themselves, which shows considerable scatter at low winds. For the stability function with the highest turbulent mixing (long tail), a lower wind speed is needed to enable a regime transition to strong inversions. By choosing various stability functions and parameter choices (not shown here), we found that S shape is a general and robust feature. Interestingly, a nonmonotonic relation between inversion strength and wind speed emerges for the cutoff function. Though, the function itself is less realistic, it will be shown that this "back folding" of the curve may also occur for realistic functions, in cases when λ is small.

Sensitivity of the model to the lumped parameter is investigated, using the short-tail function (Fig. 5). Results appear to be strongly sensitive to this parameter, representing soil and radiation feedbacks. As expected, inversions are less strong with increasing coupling strength. For large λ, the curve is "flatter" and the S shape appears less pronounced. Interestingly, the model predicts back folding for low values of λ (blue curve): a single wind

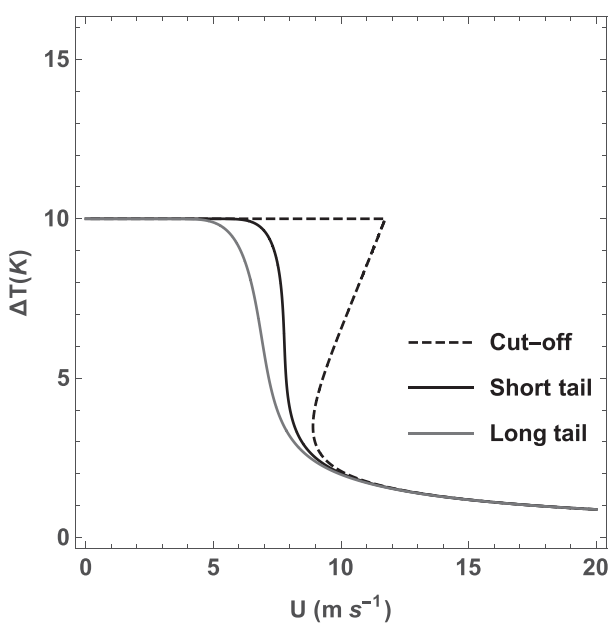

FIG. 4. Equilibrium solution of Eq. (2) for different stability functions given in Fig. 3, using the Cabauw parameters in Table 1.

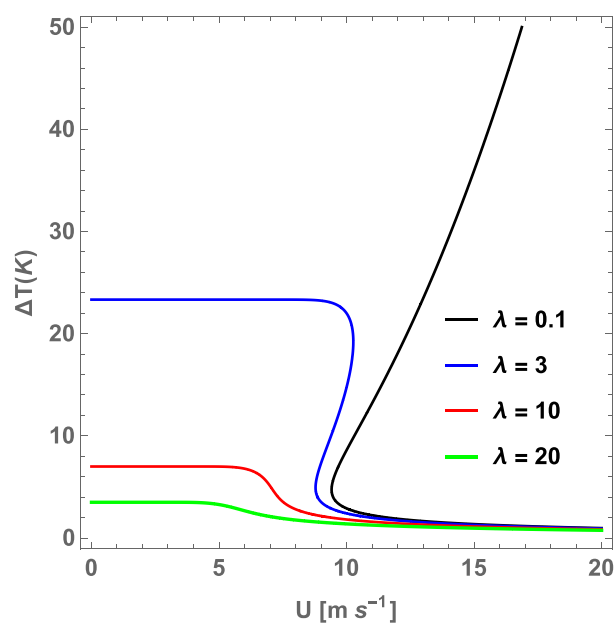

FIG. 5. Inversion strength as a function of wind speed for different values of the lumped parameter λ (W m^{-2} K^{-1}). The short-tail similarity function is used here.

speed forcing may correspond to multiple equilibria for the inversion. In this wind range, the actually observed inversion will depend on history. About 20 yr ago, McNider et al. (1995) discovered this fascinating nonuniqueness in nocturnal boundary layer equations and linked this to potential unpredictability of SBL systems [see also Shi et al. (2005)]. Here, it will be explained why nonuniqueness can exist. Also, it will be explained why this sudden regime shift must be a robust feature in nocturnal boundary layer (section 4). The case with negligible coupling strength is represented by the black line. For vanishing wind we find $\Delta T = Q_i/\lambda$ (i.e., tending to infinitely large values). In section 5 this case is discussed in the context of idealized numerical modeling over noninteractive surfaces.

b. Observational data from Dome C, Antarctica

Here, we explore the possibility of back-folding behavior from an observational viewpoint. Our model suggests that back folding may occur for low λ (i.e., with weak soil–radiation coupling). Such conditions may be encountered in Antarctica, when snow acts as an insulator and absolute temperatures and humidity (apparent emissivity) are low. Here we will present results obtained at the Antarctic station Concordia at Dome C (extensively described in, e.g., Genthon et al. 2010, 2013; Gallée et al. 2015; Vignon et al. 2017a,b). The depth of the stable boundary layer in this region is very shallow [$O(50)$ m]. This is also true for the level where the diurnal variation of wind speed is a minimum. The crossing level typically occurs at about 10 m above the surface (Vignon et al. 2017b). Figure 6a plots the temperature difference between this level and the surface as a function of wind speed at 10 m. Following Vignon et al. (2017b), data are classified into two subcategories of "radiative forcing," being the sum of net shortwave and incoming longwave radiation: $R_+ = K^\downarrow - K^\uparrow + L^\downarrow$. Here we tacitly assumed that all longwave radiation is absorbed by the surface (for Dome C: $\varepsilon_s = 0.99$). Note also that at Dome C solar elevation may be above zero at "night" when stable stratification sets in. Strongest cooling is found in cases with low incoming radiation (blue points). For this case, the maximum point density appears to describe an S-shaped curve. Also, a tendency to "fold back" seems to be present in the range between 3 and 7 m s^{-1}. However, caution for those tentative results has to be taken in view of the considerable amount of scatter in the observations.

In Fig. 6b the model result for the Dome C case is given, using parameter values given in Table 1. Note that λ, z_0, and Q_i differ from their Cabauw counterparts. The model indicates a sudden increase in inversion strength below a critical wind speed. The critical value seems to be somewhat overpredicted. The results are sensitive to

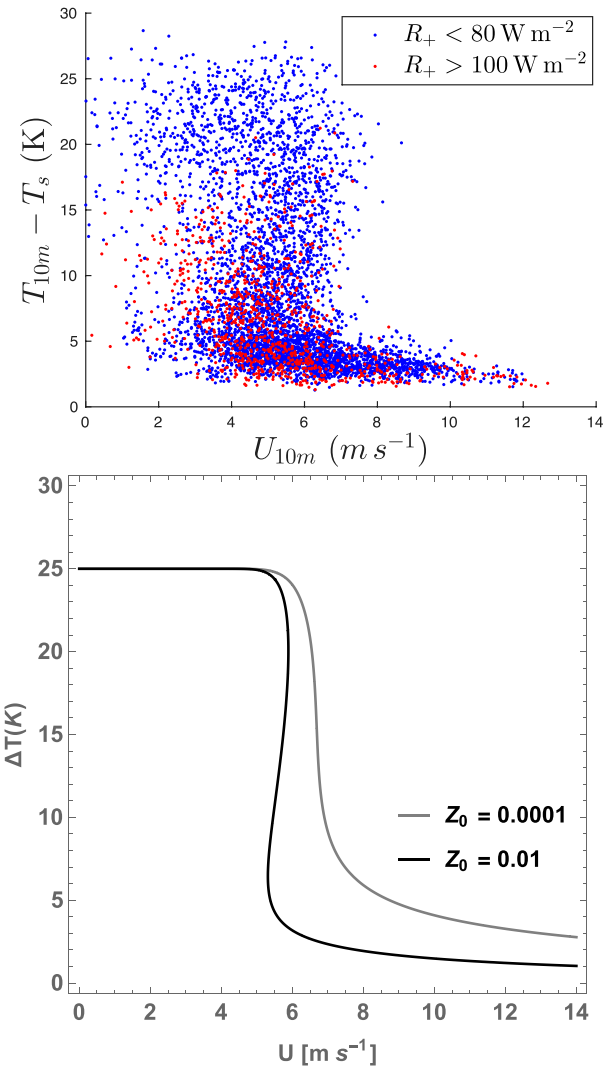

FIG. 6. (a) Temperature inversion between 10 m and the surface, as a function of wind speed as observed at Dome C. All data for the period 2014/15 in stable conditions are shown. Color coding is according to incoming radiation (see text). (b) Temperature inversion as calculated from Eq. (2) using the short-tail similarity function, with two different values of the roughness length. Input parameters as given in Table 1.

the specific choice of the roughness length. Where the back-folding effect is foreseen for larger roughness, it is not visible in the smooth-flow prediction. Though, the latter is probably more representative for Dome C, large variation in roughness length was reported by Vignon et al. (2017a). Cause of this lies in preferentially oriented snow eroded forms of 5–30 cm high, known as "Sastrugi." Depending on wind direction roughness lengths vary typically between 10^{-2} and 10^{-4} m [though "smoother" southerly flow prevailed as discussed in Vignon et al. (2017a)]. Interestingly, significant sensitivity to surface roughness was also found by Holdsworth et al. (2016) in the context

of a theoretical bifurcation analysis on stratified Couette flows, which appears to be linked [cf. also McNider et al. (1995) and Walters et al. (2007)]. As our model predictions are indicative rather than absolute, future modeling efforts with more realistic models remain necessary to clarify on this issue.

c. *Toward realistic modeling: A single-column model*

To assess generality of the results, a theoretical experiment with a multilayer single-column model is performed. We utilize the single-column version of the European Centre for Medium Range Weather Forecasts (ECMWF) Integrated Forecasting System. The model has an interactive soil–vegetation scheme. To represent the thermodynamic effect of vegetation (snow) it has a skin layer, which is coupled to the soil via an effective "skin conductivity." Radiative fluxes are calculated from a radiative transfer model (Morcrette 1991). For turbulent transport, the standard first-order scheme with a long-tail stability function (Louis 1979) was replaced by a turbulent kinetic energy scheme as described in Lenderink and Holtslag (2004) and Baas et al. (2012). Here settings according to the Third GEWEX Atmospheric Boundary Layer Study (GABLS3) model intercomparison case are used, with default parameters representative for Cabauw (Bosveld et al. 2014a). More details on the physical schemes in the model can be found online (at http://www.ecmwf.int/search/elibrary/part?solrsort=sort_label%20asc&title=part&secondary_title=31r1).

In the experiment, the model is run for different geostrophic forcings: 0.1, 2, 4, 6, 8, 10, 12, 16, and 24 m s^{-1}. For each run the strength of the inversion between the 40-m level and the surface is diagnosed in the time frame between 0000 and 0300 UTC (i.e., when "steady state" has set in). The results are shown in Fig. 7, with red points indicating the default runs. For comparison, the results with reduced surface coupling (in blue) and with a long-tail stability function (Louis 1979) are given (in green) as well.

The enveloping curve through the red point resembles the observational wind dependence in Fig. 1. Again an S-shaped curve is found, and the maximum inversion strength of $O(10)$ K for the Cabauw case is well captured. The transition zone, on the other hand, seems to be broader in the simulations than in the observations. This is even more so with the long-tail stability function (green). This broadening effect by stability functions with enhanced turbulent mixing is comparable to the sensitivity of the conceptual model to turbulent exchange functions as presented in Fig. 4. As this type of stability functions is mostly used in global climate models this result has strong implications for the capability of those to simulate observed temperature tendencies. As discussed in McNider et al. (2012) and Walters et al. (2007),

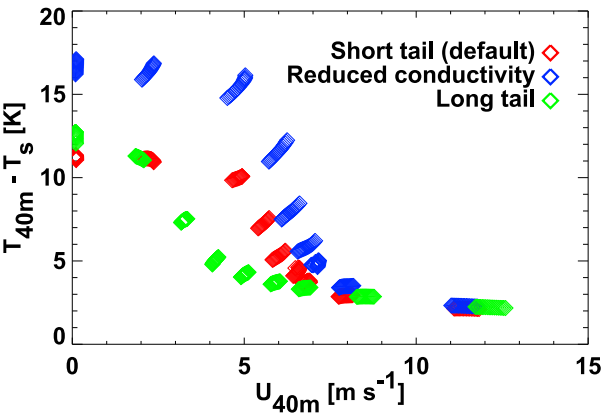

FIG. 7. Inversion strength between 40 m and the surface as a function of the wind speed at 40 m as simulated by the ECMWF-IFS column model using default settings for Cabauw (see text). Results between 0000 and 0300 UTC are shown. Along with the default case (red dots), results from simulations with a long-tail stability function (green) and a reduced skin conductivity are shown (blue).

observed warming tendencies at screen level over the last century are much larger for the nighttime minimum temperature T_{min} than for the daytime maximum temperature T_{max}. As a result, the diurnal temperature range has largely decreased in observations (Vose et al. 2005; Caesar et al. 2006). The fact that GCMs are presently unable to capture this effect could (partly) be related to their inability to model sharp regime transitions that appear to be present in observations (Figs. 1 and 6). More specifically, our analysis in section 5 [Fig. 9 and Eq. (6)] will show that in a dimensionless framework a decrease in isothermal net radiation (in response to enhanced emission of greenhouse gases) has a similar effect as an increase in wind speed. From Fig. 7 it is clear that with increasing wind the decrease in inversion strength (warming of the surface) is much less with enhanced mixing formulations than with the more realistic scheme. As large part of polar regions will reside in the "steep part of the S curve" (Fig. 6), indeed strong response of nighttime surface temperatures can be expected in reality. GCMs may therefore need to maintain those abrupt transitions seen in observations (R. T. McNider and A. H. Monahan 2016, personal communication). However, a full discussion is beyond the scope of the present text.

To assess the impact of surface coupling, a second numerical experiment was performed, in which the skin conductance was reduced by a factor of 10 (blue points). Now the transition between the two inversion regimes is much sharper. The maximum inversion strength has also increased by 50%. Notice that in this case, even with negligible skin conduction, negative feedbacks in the radiative scheme limit the maximum inversion to ~17 K. Though skin conductivity is different from our lumped

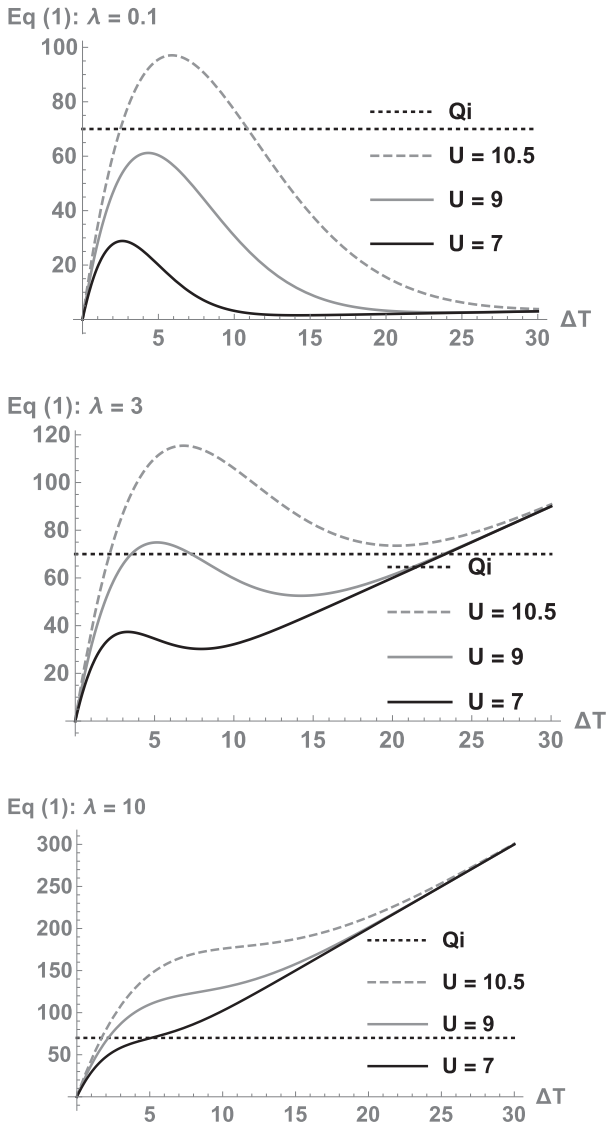

FIG. 8. Magnitude of terms in Eq. (2) as a function of inversion strength and wind speed, using the short-tail similarity function. Intersections of horizontal energy demand line Q_i with curved lines (sum of supply terms: turbulent and "conductive" heat fluxes) represent equilibrium points. (a) "No coupling," (b) weak coupling, and (c) strong coupling.

parameter, the experiment suggests general validity of the feedback mechanism. In the future, a more in-depth study is foreseen [with attention to implementation aspects suggested by Mackaro et al. (2012)]. In the next section, the role of physical feedbacks on the regime transition is studied in detail.

4. Regime transition: The role of physical feedbacks

The previous examples indicate that a sudden increase in temperature inversion may occur in a certain wind range. We start from the maximum sustainable heat flux theory, which was developed for flux-driven systems without atmosphere–land coupling (Van de Wiel et al. 2007; VdW12a,b). It will be shown that similar physics hold for coupled systems.

In Fig. 8 terms of Eq. (2) are plotted as functions of inversion strength and wind speed, using the short-tail similarity function. The dotted line is the surface energy demand Q_i, whereas the curved lines represent the heat supply (sum of turbulent and "conductive" fluxes). The panels correspond to different values of λ. The intersection points represent the equilibria. We consider the case with negligible coupling: $\lambda = 0.1$ (Fig. 8a). The heat supply strongly depends on the wind strength, as the maximum turbulent heat flux $H_{\max} \propto U^3$ (Taylor 1971; Malhi 1995; Delage et al. 2002; VdW12b). There is a minimum wind speed such that equilibrium can be reached. For weaker winds, even the maximum supply is insufficient to compensate for the loss, such that extreme cooling will occur (off-scale in Fig. 5). Because of the strong wind speed dependence, the critical wind itself is sharply defined. As such, the threshold is robust and only weakly sensitive to specific closure details or parameter values (apart from surface roughness).

In Fig. 8b the lumped parameter is small, but nonnegligible (as for conditions at the Antarctic Plateau). Now, "unbounded" cooling does not occur and even for subcritical winds an equilibrium is found. Consider the $9\,\mathrm{m\,s^{-1}}$ case for which three equilibrium points are found. At the left-hand side the equilibrium occurs for $\Delta T \approx 4\,\mathrm{K}$ (i.e., a weak inversion). A slight decrease of the wind would, however, make this equilibrium disappear and only the solution with the strong inversion will remain $\Delta T \approx 24\,\mathrm{K}$. This explains why the regime transition in the inversion strength occurs over a narrow wind range, such as in the Antarctic case depicted in Fig. 6.

Finally, in Fig. 8c the case with a moderately large λ value is discussed (as for Cabauw). The influence of the linear term in Eq. (2) is now much larger, which makes the transition smoother. The maximum difference in inversion strength becomes much smaller. Yet, even in this case, the role of the turbulent heat flux is still evident, resulting in a well-defined transition zone.

It is important to realize that the equilibrium points in Fig. 8 are linked Fig. 5. In Fig. 5 one can find the same points by drawing an imaginary vertical line at the corresponding wind speed. At the intersection of this line with the curve of corresponding λ in Fig. 5, the equilibrium points of Fig. 8 reappear. To clarify, an example is given: in Fig. 8b, at a wind speed of $9\,\mathrm{m\,s^{-1}}$ three

equilibrium values for the inversion strength are found. The same three values are found as intersects in Fig. 5, if one takes a vertical slice at $U = 9\,\mathrm{m\,s^{-1}}$. As such, nonmonotonic behavior in Fig. 8 is translated in multivalued solutions of the S curve in Fig. 5. Likewise, monotonic behavior is found in both figures when λ is large.

To summarize this section, because of the dominant wind speed sensitivity, the MSHF mechanism remains a driving factor behind the sharp regime transitions of the inversion strength, both in idealistic flux-driven systems as in realistic surface-coupled systems.

5. The transition wind speed

From our previous analysis it appears that there is a characteristic wind speed that announces a rapid change of the inversion strength. We refer to this as the transition wind speed. Here, we look for methods to quantify this parameter in terms of surface coupling strength and forcing parameters. For the noncoupled case an analytical expression was derived in VdW12a,b:

$$U_{\min} = \left\{ \frac{27}{4} \frac{\alpha g}{T_r \kappa^2} \frac{|Q_n| - |G|}{\rho c_p} z_r [\ln(z_r/z_0)]^2 \right\}^{1/3}. \quad (5)$$

In VdW12a,b, the transition speed was referred to as "the minimum wind speed for sustainable turbulence" $U_{\min}$ to indicate that, in absence of coupling, no equilibrium is found when the wind speed drops below this threshold (cf. the black line in Fig. 5). Feedbacks were pragmatically "included" by assuming net radiation Q_n and soil heat flux G to be known parameters. To apply Eq. (5) one needs to provide an estimate for $|Q_n| - |G|$, being the "flux demand" at the surface. This loss has to be compensated by turbulent heat as to prevent rapid surface cooing. In VH15, a value of $10\,\mathrm{W\,m^{-2}}$ was used as a conservative estimate for the demand under clear skies.

In reality, however, Q_n and G are internal parameters, which depend on surface temperature itself. Therefore we prefer to use isothermal net radiation Q_i as an external parameter and calculate internal feedbacks explicitly using the lumped parameter model. To facilitate analysis, Eq. (2) is nondimensionalized. Our main external parameters are $Q_i, U(z_r)$, z_r, z_0, C_v, and λ. Key parameter in our scaling is the flux-based velocity scale (see VH15):

$$v_* = \left(\frac{g}{T_r} \frac{Q_i}{\rho c_p} z_r \right)^{1/3}. \quad (6)$$

From this, the typical temperature scale $T_{\mathrm{sc}} = Q_i/(\rho c_p v_*)$ and time scale $t_{\mathrm{sc}} = C_v/(\rho c_p v_*)$ are defined. Next, we substitute $\hat{U} = U/v_*$, $\hat{T} = T/T_{\mathrm{sc}}$, and $\hat{t} = t/t_{\mathrm{sc}}$ in Eq. (2) and obtain

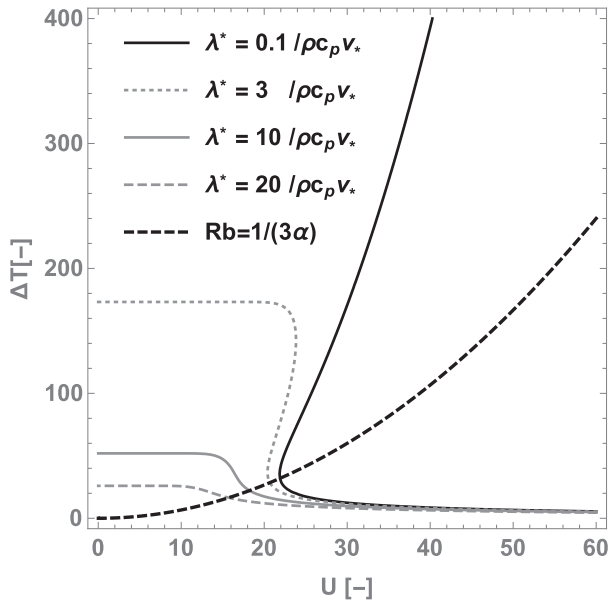

FIG. 9. Nondimensional inversion strength as function of wind speed. Dashed line represents $\hat{R}_b = 1/3\alpha$.

$$\frac{d\Delta\hat{T}}{d\hat{t}} = 1 - \lambda^* \Delta\hat{T} - c_D \hat{U} \Delta\hat{T} f(\hat{R}_b), \quad (7)$$

with $\hat{R}_b = \Delta\hat{T}/\hat{U}^2$. Besides the bulk Richardson number, three dimensionless groups result. Surface friction is incorporated via the drag coefficient c_D and soil–radiation feedbacks are represented by the normalized lumped parameter $\lambda^* = \lambda/(\rho c_p v_*)$. Wind forcing is represented by $\hat{U}$. In Van Hooijdonk et al. (2015) this nondimensional parameter was introduced as the shear capacity of the flow (SC). Stationary solutions are depicted in Fig. 9 as a dimensionless equivalent of Fig. 5. For interpretation purposes also the line $\hat{R}_b = 1/3\alpha$ is plotted.

In our analysis we now use $f(\hat{R}_b) = (1 - \alpha\hat{R}_b)^2$, which is close to the short-tail function. In the uncoupled system with $\lambda^* = 0$, the minimum wind speed is given by

$$\hat{U}_{\min,0} = \left(\frac{27}{4} \frac{\alpha}{c_D} \right)^{1/3}. \quad (8)$$

(appendix A). The subscript 0 is indicates that the lumped parameter is zero. By multiplication of this equation with v_* it is readily seen that the solution is equivalent to (5), but now with Q_i instead of $|Q_n| - |G|$. However, this similarity is merely mathematical as Q_i attains much larger values.

In the uncoupled case a transition occurs when the turbulent heat flux maximizes at equilibrium. It can be

proven that then $\hat{R}_b = 1/3\alpha$. Also in the general case, a transition is expected when the turbulence contribution is near its maximum (cf. Fig. 8b). Next, we put the ansatz that the transition occurs at $\hat{R}_b \approx 1/3\alpha$. Indeed, intersection of this line with the equilibrium curves supports this assumption, in a sense that rapid change of inversion is found. The expression for the transition wind becomes

$$\hat{U}_{\min,\lambda} \approx \hat{U}_{\min,0}\left[1 - \frac{1}{2 + 3\hat{U}_{\min,0}(4/9)(c_D/\lambda^*)}\right]. \quad (9)$$

The "almost equal to" symbol is used to indicate that the analytical solution is an approximation (appendix A). One can readily verify that the solution converges to $\hat{U}_{\min,0}$ in the case $\lambda^* \to 0$. Using the Cabauw parameter values of Table 1 and λ values $\lambda = (0.1, 3, 10, 20)$, this gives $\hat{U}_{\min,\lambda} = (22.1, 20.9, 18.9, 17.1)$ and dimensional values $U_{\min,\lambda} = (9.5, 9.0, 8.1, 7.4)\,\mathrm{m\,s^{-1}}$. Comparison with Figs. 9 and 5 indicates that Eq. (9) provides a useful estimate except for the largest λ value, for which a numerical solution is preferred over the analytical approximation.

6. Perturbation analysis and stability

a. *The heat flux paradox*

In Van de Wiel et al. (2007, hereafter VdW07) a multilayer analog to our "no feedback" one was analyzed with similar figures as Fig. 8a. In their work it was argued that only the equilibrium at the left-hand side of the heat flux maximum is hydrodynamically stable in a sense that solutions will be attracted to their equilibrium after a perturbation. The right-hand-side equilibrium is unstable and solutions divergence from their equilibrium after perturbation. As such, time-integrated model solutions will only result in a single-branched equilibrium curve. This prediction was confirmed in direct numerical simulation studies on flux-driven idealizations of stratified flows without surface coupling (Donda et al. 2015, 2016; Van Hooijdonk et al. 2017). Holdsworth et al. (2016) formalized and extended the mathematical findings of VdW07 and confirmed single branching in noncoupled, flux-driven systems.

In reality, however, atmospheric coupling with the surface is a realistic feature. Moreover, analysis of the CASES-99 field experiment in VdW07 indicates that both branches of the heat flux curve exist in atmospheric observations of turbulent fluxes near the surface. Monahan et al. (2015) used hidden Markov models for an in-depth analysis of Cabauw data. They revealed that indeed two distinct branches exist in observations and that those branches correspond to two different statistical sets. Also for other locations evidence for double-branched behavior in atmospheric observations has been presented (e.g., Grachev et al. 2005; Sorbjan 2006; Mahrt et al. 1998; Basu et al. 2006). Here we investigate the reason for this (apparent) discrepancy between VdW07 and the observations and refer to this as the "heat flux paradox."

Basu et al. (2008) suggested that the solution lies in the boundary condition chosen. Indeed, by replacing the flux condition with a temperature condition, two branches are simulated as in observations. A similar suggestion was made by Gibbs et al. (2015). However, they were incorrect in their interpretation of VdW07 by suggesting that root-finding algorithms of steady states/numerical issues are responsible for the nonrepresentation of a second equilibrium branch in that work. Steady-state analysis cannot provide information about the stability of a system as the latter results from dynamics. Moreover, (in)stability of stratified boundary layers arises from physics (i.e., nonlinear diffusion) rather than from numerics (Derbyshire 1999a,b): it is possible to prove marginal stability/instability from mathematical analysis alone, without relying on numerical solving techniques. To clarify on this issue some examples will be given below.

At the same time, we recognize that a change of boundary conditions may have a dramatic impact on the physical stability of a system and that simulations with a prescribed surface temperature may show double-branched solutions. But, although more attractive on this aspect, such alternative configuration does not automatically lead to more physical solutions. Holtslag et al. (2007) point out that surface temperature itself is an internal variable of the system, which is not known a priori (except maybe in case of melting snow). By imposing the temperature tendency, one can create artificial cases, which do not present reality. It is, for example, unlikely that a surface tendency of $3\,\mathrm{K\,h^{-1}}$ would occur in cases when the geostrophic wind amounts to $15\,\mathrm{m\,s^{-1}}$. In our opinion, flux and temperature boundary conditions are both strong idealizations, which may provide useful benchmarks to facilitate theoretical research (e.g., Huang and Bou-Zeid 2013; Ansorge and Mellado 2014; Sullivan et al. 2016). For one-to-one comparison with reality, however, caution has to be taken.

Below, we try to understand the more general case, by replacing the aforementioned flux/temperature conditions by a rudimentary energy balance. Instead of analyzing Eq. (2) directly, we will simplify it to its mathematical essence, leaving out all unnecessary details. This allows in-depth analysis of the instability mechanism. It will be shown that the strength of the surface coupling decides on the stability and the branching behavior.

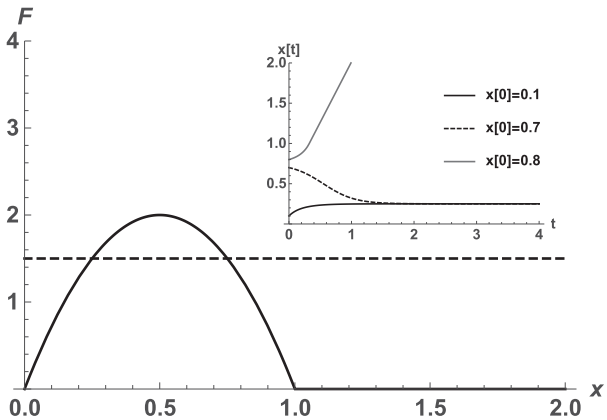

FIG. 10. Case without coupling. Magnitude of energy demand (dashed line) and supply (solid line) as function of x according to Eq. (10). Equilibria are represented by two intersection points of the parabola with the horizontal line. (inset) Time integrations for different initial conditions.

Our simplified model reads

$$\frac{dx}{dt} = Q_i - \lambda x - Cx(1-x). \tag{10}$$

The symbol x represents ΔT, and $f(x) = (1-x)$ represents the linear form of the stability function, truncated for $x > 1 \rightarrow f(x) = 0$ (as in Fig. 3). Note that with this form is preferred over, for example, $f(x) = (1-x)^2$ as one avoids mathematical complexity (cubic equation), while maintaining the essential physical feedback mechanism. Our results below are mathematical analogs to the fixed wind cases in Fig. 8. Again, three cases with different coupling strengths are considered:

1) No coupling. We consider the case with $\lambda = 0$, $Q_i = 3/2$, and $C = 8$ (specific numbers are chosen for mathematical convenience only, without loss of generality). The "demand" and "supply" are plotted as a function of x (Fig. 10). Two equilibrium solutions are obtained: $x_{eq} = 1/4$ and $x_{eq} = 3/4$. We investigate if those points are stable to perturbations. Equation (10) is numerically integrated in time using different initial conditions (figure inset). Solutions are attracted by the lhs equilibrium (stable) and repelled by its rhs counterpart (unstable).
Next, we use linear perturbation analysis to prove this finding. Close to the equilibrium we may use $x \approx x_{eq} + \delta x$. Substitution in Eq. (10) and rearranging gives

$$\frac{d(\delta x)}{dt} = \left[\frac{3}{2} + 8x_{eq}^2 - 8x_{eq}\right] - 8(\delta x)(1 - 2x_{eq}) + 8(\delta x)^2, \tag{11}$$

where we used $dx_{eq}/dt = 0$. The term in the square brackets in Eq. (11) is zero by definition. We linearize by ignoring the quadratic term and substitute $x_{eq} = 1/4$. The solution reads

$$\delta x(t) = \delta x(0)\exp(-4t) = \delta x(0)\exp(-t/\tau), \tag{12}$$

with recovery time scale $\tau = 1/4$. The amplitude of the initial perturbation decreases and the equilibrium is stable. Substitution of $x_{eq} = 3/4$ in Eq. (11) gives an opposite sign in the argument of the exponent (instability). The sign change takes place at the maximum ($x_{eq} = 1/2$). The lhs branch of the energy supply is stable and the rhs is unstable (QED).

2) Weak coupling. Next, a case is considered with $\lambda = 2$, $Q_i = 3$, and $C = 8$ (Fig. 11). Three equilibrium points are found: $x_{eq} = 1/2$, $3/4$, and $3/2$. A local maximum appears at $x = 5/8$. Again, numerical time integration support stable and unstable equilibria at the lhs and rhs of the maximum of the parabola, respectively. The third point is stable and acts as an attractor for perturbations at the rhs of the middle point.
Following the same procedure as before we find for $x < 1$

$$\frac{d(\delta x)}{dt} \approx -2(\delta x)(5 - 8x_{eq}) \tag{13}$$

and for $x > 1$

$$\frac{d(\delta x)}{dt} = -2(\delta x), \tag{14}$$

with solutions analog to (12), with $\tau = 1/2$. By inspecting the signs we find that exponential growth is found for $5/8 < x < 1$ and decay elsewhere. A positive slope of the curve appears to correspond to stable branches and negative slopes to unstable branches. In appendix B a mathematical proof for this conjecture—which is also applicable to, for example, Fig. 8—is given. The recovery time scale τ is related to the magnitude of the

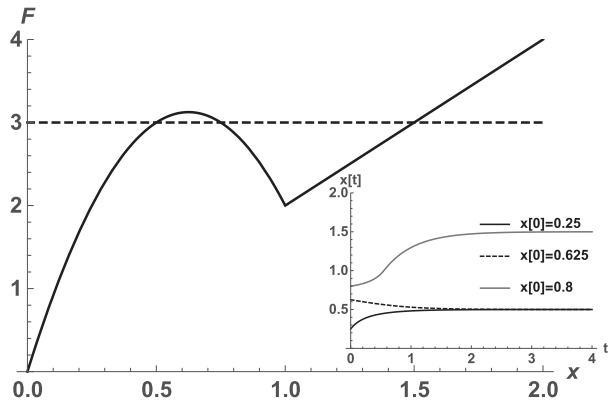

FIG. 11. As in Fig. 10, but for case with weak coupling.

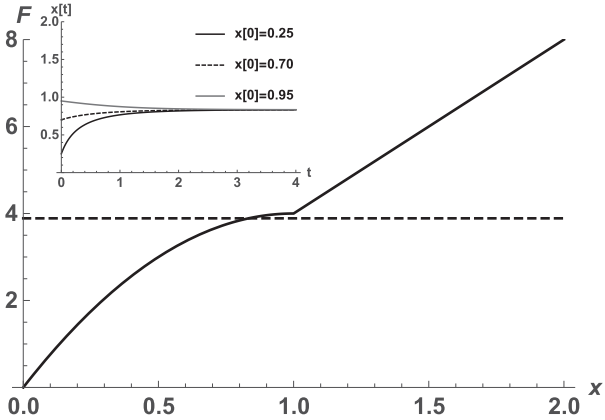

FIG. 12. As in Fig. 10, but for case with strong coupling.

slope of the curve in the equilibrium point via $\tau = 1/|F'(x_{eq})|$.

3) Strong coupling. Finally, we discuss the case $\tau = 4$, $Q_i = 35/9$, and $C = 4$ (Fig. 12).
This case, having a positive slope everywhere, is representative for most atmospheric cases. Equilibrium solutions are unconditionally stable; that is, having

$$\frac{d(\delta x)}{dt} \approx -8(\delta x)(1 - x_{eq}), \tag{15}$$

and for $x > 1$,

$$\frac{d(\delta x)}{dt} = -4(\delta x). \tag{16}$$

A unique equilibrium is found at $x_{eq} = 5/6$ and it corresponds to $\tau = 3/4$. We note that a special case occurs at $Q_i = 4$, when $x_{eq} = 1$. In that particular case, positive and negative perturbations respond with different time scales because of the (artificial) discontinuity in the slope (appendix B).

Now it is possible to solve the heat flux paradox. In the strongly coupled case (like the Cabauw case), $dF/dx > 0$ ($\forall x$ except for $x = 1$). The monotonicity implies that all points are stable. This impacts on the heat flux graphs as follows. Suppose that like in the insets of Figs. 10–12, one performs time integrations starting from neutral conditions. One repeats this exercise for many Q_i values. Next, one diagnoses $4x_{eq}(1 - x_{eq})$ (i.e., the heat flux) as a function of the equilibrium x_{eq}. The full parabolic heat flux curve is found, as in the aforementioned experimental studies. In contrast, in the noncoupled case dF/dx is positive for $x < 1/2$ only. Only half the curve can emerge from a similar time-integration exercise, as found in flux-driven noncoupled model simulation studies. Finally, in the intermediate case of weak coupling, only part of the curve is found according to our model. In Antarctic case, this would imply that the unstable back-folding branch of the S curve would be unstable. Indeed, analysis by Vignon et al. (2017b) shows that those points behave systematically less stationary compared to the stable branches and hence appear to be less stable. Still the unstable branch is "well populated" by points, which could imply that growth rates of instabilities remain small as suggested by Holdsworth et al. (2016). On the other hand, it should also be realized that our model may be oversimplified to capture subtle effects as depicted in Fig. 6a, because it misses potentially important negative feedbacks in the momentum dynamics (cf. Derbyshire 1999b).

To summarize, the strength of the coupling decides on the observed range of the parabolic heat flux curve. As strong coupling prevails (except for snow-covered surfaces), the full curve is found in most atmospheric observations. In idealized, noncoupled simulations with flux-driven boundary conditions, only half of the curve is observed.

b. *The recovery time scale in relation to observational scatter*

The observational examples in Figs. 1 and 6a show an interesting feature. Apart from the fact that the inversion itself increases rapidly below the critical wind speed, the observational scatter seems to increase suddenly at this point as well. This can partly be explained from the (trivial) fact that the curve is almost vertical in this narrow wind regime: a small observational error in wind will result in a large uncertainty in the inversion. Here, a second reason for the increase in scatter is given. Again, Eq. (10) is used as an analog. It will be shown that the "recovery time" of the system in response to perturbations is large near the critical wind. This leaves natural fluctuations to be largely undamped, so that they tend to persist. Our results are meant as a first-order analysis. For a more conclusive analysis on this interesting aspect, in-depth observational analysis is required in the future.

We discuss the strongly coupled case, as it is most representative for the atmosphere. Apart from perturbation analysis, information on response times is also available from closed-form solutions. For $\lambda = 4$, $Q_i = 35/9$, and $C = 4$, and $x[0] = 0$, we find for $x < 1$

$$x[t] = \frac{35}{6}\frac{(e^{4/3t} - 1)}{(7e^{4/3t} - 5)}. \tag{17}$$

The characteristic time scale is $\tau = 3/4$ in accordance with our previous results. Observe that $t \to \infty$ for $x \to x_{eq} = 5/6$.

Next, we repeat this exercise for different values of Q_i, as if we shift the dashed line in Fig. 12 vertically and diagnose τ. The result is given in Fig. 13.

Instead of Q_i we choose to plot its inverse in order to facilitate interpretation. As expected, the response time τ is related to the slope in Fig. 12. An exception must be made for $Q_i = 4$ and $x_{eq} = 1$. As the slope vanishes, the response time would be infinite. However, in this case second-order effects cannot be ignored in the stability/time scale analysis. In fact, the closed-form solution with $x[t = 0] = 0$ indicates algebraic, rather than exponential, adjustment:

$$x[t] = \frac{4t}{1 + 4t}. \tag{18}$$

The adjustment time τ is small for large $1/Q_i$ (weak cooling) and large for small $1/Q_i$. A maximum occurs near the "critical point" $1/Q_i = 1/4$. We reconsider Fig. 9 and realize that a decrease in Q_i has a similar effect as an increase in wind speed. Indeed, in our dimensionless framework it is the ratio of wind speed to $Q_i^{1/3}$ that decides on the regime (hence the statement in section 3 that an increase in GHG emission will have an effect similar to a wind speed increase in a dimensionless context). For here, the bottom line is that we may compare the horizontal axes in Figs. 13 and 9 as being qualitatively similar.

In our atmospheric model of Eq. (2), characteristic time scales are readily found by considering limit cases. For vanishing wind, a constant time scale of $\tau = C_v/\lambda$ is predicted. For high winds we find $\tau = C_v/(\rho c_p U)$ (i.e., a hyperbolic wind speed dependence). Those effects are also visible in Fig. 13. Because of the aforementioned "slope-time scale" relation, a maximum around the critical wind speed will be found in the atmospheric case as well. Long adjustment times imply that perturbations from equilibrium may persist for some time. On the right close to the critical speed, the "resilience of the system" is low. The opposite is true for high wind speeds, where the system reacts fast to perturbations. It is a common experience in observational analysis that scatter increases rapidly, by going from weakly to very stable cases. The current analysis may provide a logical explanation for this. However, as explained by Mahrt (2014) other (phenomenological) aspects may play an important role as well, so that more analysis on this issue is required in the future.

7. Conclusions

In this study we use a conceptual atmospheric–surface model to understand regime transitions in near-surface inversions. The model combines a surface energy budget with a bulk parameterization for turbulent transport. Instead of parameterizing soil heat transport and the radiative balance separately, both feedbacks on the system are combined in an empirical way by introducing a so-called lumped parameter. As previous theoretical analysis by the present authors largely ignored those important feedbacks, present work represents a more realistic extension of that framework.

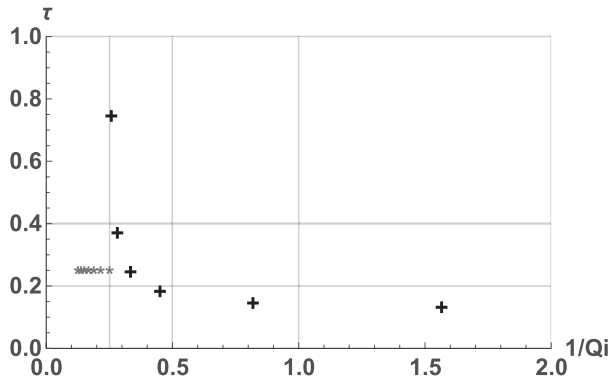

FIG. 13. Strongly coupled case: characteristic time scale as a function of inverse "cooling." The highest point shown corresponds to $\tau = 3/4$ for $1/Q_i = 9/35$. Cross symbols refer to weakly cooled cases ($1/Q_i > 1/4$ and $x_{eq} < 1$; see Fig. 12). Asterisks refer to $1/Q_i < 1/4$ and $x_{eq} > 1$.

In nocturnal boundary layer observations, often a sharp transition is found when plotting the strength of the steady-state inversion as a function of the ambient wind speed. This typically results in an S-shape dependency between both quantities. As expected, inversions are weak for strong winds, whereas large inversions are found at weak winds. However, the transition between those states occurs over a rather narrow wind range.

The present models explain this fascinating behavior. It is shown that the mechanism for sudden transition can be understood in terms of the maximum sustainable heat flux mechanism. The existence of the S shape in observations appears to be robust in a sense that it is observed in Cabauw data (moderate climate) as well as for data obtained at Dome C, Antarctica. Differences between the two sites were explained by a dissimilar strength of atmosphere–surface coupling, being much weaker in the latter case. Interestingly, qualitative support on generality of the results was obtained by running a more realistic, multilayer column model for strong and weak coupling, which leads to similar conclusions.

In the second part of the paper, model equations were studied in depth, using linear perturbation analysis. An important paradox on the existence of the so-called heat flux duality was solved. In observations, the same value of the turbulent heat flux may occur at weak and strong static stability. Yet, in flux-driven simulations without

surface coupling, only the weakly stable part is found. Here, we show that both cases are specific realizations of a more general case. It is the coupling strength, which ultimately decides on which part of the heat flux curve will be observed. As such, the aforementioned numerical results are not in contradiction with the observations.

An interesting finding in the analysis is related to the so-called recovery time scale to perturbations. In observations, the amount of scatter appears to increase rapidly in the transition range. Model dynamics reveal that in this range the recovery time scale is at its maximum. This implies that natural fluctuations away from the equilibrium are only weakly damped, such that indeed larger scatter can be expected. A recent study by the present authors (Van Hooijdonk et al. 2017) suggests that analysis of this recovery time scale could be used as a potential "early warning signal" of a nearing regime transition. More experimental data analysis is needed for a conclusive analysis on this interesting aspect. Additionally, our results would largely benefit from studies similar to the present one, using mesoscale model analysis and/or large-eddy simulation in combination with observational data.

Acknowledgments. The scientific comments on the original manuscript by Dick McNider, Adam Monahan, and John Wyngaard are highly appreciated. The research is supported by a Consolidator Grant of the European Research Council (648666) and Grant 82301010 from the Dutch National Science Foundation (NWO), which is gratefully acknowledged. The Dome C observatory of the surface atmospheric boundary layer is supported by IPEV (program CALVA 1013), INSU/LEFE (GABLS4 and DEPHY2), and OSUG (GLACIOCLIM). We thank the BSRN network and particularly C. Lanconelli for the dissemination of radiation data at Dome C.

APPENDIX A

Derivation of the Minimum Wind Speed

A derivation of expressions (8) and (9) is given. In Eq. (7) we consider the stationary case with $\lambda^* = 0$ and $f(\hat{R}_b) = (1 - \alpha\hat{R}_b)^2$. Multiplication with $\alpha/(c_D\hat{U}^3)$ gives

$$\frac{\alpha}{c_D\hat{U}^3} = \alpha\hat{R}_b \times (1 - \alpha\hat{R}_b)^2. \tag{A1}$$

Essentially, this is the energy demand (lhs) and supply (rhs). This steady-state equation is fully equivalent to Eq. (11) in VdW07 and Eq. (17) in Holdsworth et al. (2016). With respect to the first, the equilibrium curve is given by $\hat{H} = \hat{u}_*^3 - \hat{u}_*^2$. The sign of the heat flux is negative and hats represent different normalizations; for example, in VdW07, $\hat{u}_* = (u_*/\kappa U)\ln(z/z_0) = 1 - \alpha R_b$ (using the quadratic stability function). Substituting for the surface flux $(-Q_i)$ equivalence can be proven straightforwardly. The critical state occurs when the source term maximizes at equilibrium, which occurs at $\alpha\hat{R}_b = 1/3$ (cf. Fig. 8a). The maximum supply amounts to $4/27$. Solving for wind speed,

$$\hat{U}_{\mathrm{min0}} = \left(\frac{27}{4}\frac{\alpha}{c_D}\right)^{1/3}. \tag{A2}$$

Next, we generalize for nonzero λ values. Because of wind speed sensitivity, we again expect the transition to occur near the point where the turbulent heat flux contribution is maximum (i.e., near $\alpha\hat{R}_b = 1/3$). Next, we use this as an ansatz. We now define the transition point as the intersect of the equilibrium (S) curve with the $\alpha\hat{R}_b = 1/3$ line (black dashed line in Fig. 9). Inserting in Eq. (7) at equilibrium and rewriting gives

$$0 = 3\alpha - \lambda^*\hat{U}^2 - \frac{4}{9}c_D\hat{U}^3. \tag{A3}$$

Though this cubic equation could be solved for $\hat{U}$ (e.g., Abramowitz and Stegun 1965), the complexity of the result would add little to a numerical solution. We therefore approximate by $\hat{U}_{\mathrm{min},\lambda} \approx \hat{U}_{\mathrm{min},0}(1 + \varepsilon)$, with $\hat{U}_{\mathrm{min},0}$ given by Eq. (8). Next, we use $(1 + \varepsilon)^n \approx 1 + n\varepsilon$ for $\varepsilon \ll 1$. Substitution leads to the solution in Eq. (9). Note that in our case ε is negative. For $\lambda = (0.1, 3, 10, 20)$, $\varepsilon = -(0.002, 0.06, 0.15, 0.23)$.

APPENDIX B

Generalization of the x Problem

The analysis of section 6 is generalized by defining $dx/dt = -F(x)$. The minus sign is taken for convenience so that results can be interpreted in terms of Figs. 10–12, in which the last two terms of Eq. (10) are given a positive sign. After linearization around equilibrium, using $F(x_{\mathrm{eq}}) \equiv 0$ we find $d(\delta x)/dt \approx -F'(x_{\mathrm{eq}})(\delta x)$, with $F'(x_{\mathrm{eq}})$ the derivative of with respect to x in the equilibrium point. The solution is $\delta x(t) = \delta x(0)\exp[-tF'(x_{\mathrm{eq}})]$, which is used in section 6.

REFERENCES

Abramowitz, M., and I. A. Stegun, 1965: *Handbook of Mathematical Functions with Formulas, Graphs, and Mathematical Tables.* Dover, 1046 pp.

Acevedo, O. C., F. D. Costa, and G. A. Degrazia, 2012: The coupling state of an idealized stable boundary layer. *Bound.-Layer Meteor.*, **145**, 211–228, doi:10.1007/s10546-011-9676-3.

——, L. Mahrt, F. S. Puhales, F. D. Costa, L. E. Medeiros, and G. A. Degrazia, 2016: Contrasting structures between the decoupled and coupled states of the stable boundary layer. *Quart. J. Roy. Meteor. Soc.*, **142**, 693–702, doi:10.1002/qj.2693.

Ansorge, C., and J. Mellado, 2014: Global intermittency and collapsing turbulence in the stratified planetary boundary layer. *Bound.-Layer Meteor.*, **153**, 89–116, doi:10.1007/s10546-014-9941-3.

Baas, P., B. J. H. van de Wiel, L. van de Brink, and A. A. M. Holtslag, 2012: Composite hodographs and inertial oscillations in the nocturnal boundary layer. *Quart. J. Roy. Meteor. Soc.*, **138**, 528–535, doi:10.1002/qj.941.

Basu, S., F. Porté-Agel, E. Foufoula-Georgiou, J.-F. Vinuesa, and M. Pahlow, 2006: Revisiting the local scaling hypothesis in stably stratified atmospheric boundary layer turbulence: An integration of field and laboratory measurements with large-eddy simulations. *Bound.-Layer Meteor.*, **119**, 473–500, doi:10.1007/s10546-005-9036-2.

——, A. A. M. Holtslag, B. J. H. van de Wiel, A. F. Moene, and G.-J. Steeneveld, 2008: An inconvenient ''truth'' about using sensible heat flux as a surface boundary condition in models under stably stratified regimes. *Acta Geophys*, **56**, 88–99, doi:10.2478/s11600-007-0038-y.

Beven, K., 2001: *Rainfall-Runoff Modeling: The Primer.* Wiley, 372 pp.

Blackadar, A. K., 1957: Boundary layer wind maxima and their significance for the growth of nocturnal inversions. *Bull. Amer. Meteor. Soc.*, **38**, 283–290.

Bosveld, F. C., P. Baas, E. M. van Meijgaard, E. I. F. de Bruijn, G. J. Steeneveld, and A. A. M. Holtslag, 2014a: The third GABLS intercomparison case for evaluation studies of boundary-layer models. Part A: Case selection and set-up. *Bound.-Layer Meteor.*, **152**, 133–156, doi:10.1007/s10546-014-9917-3.

——, and Coauthors, 2014b: The third GABLS intercomparison case for evaluation studies of boundary-layer models. Part B: Results and process understanding. *Bound.-Layer Meteor.*, **152**, 157–187, doi:10.1007/s10546-014-9919-1.

Caesar, J., L. Alexander, and R. Vose, 2006: Large-scale changes in observed daily maximum and minimum temperatures: Creation and analysis of a new gridded data set. *J. Geophys. Res.*, **111**, D05101, doi:10.1029/2005JD006280.

Delage, Y., P. A. Bartlett, and J. H. McCaughey, 2002: Study of 'soft' night-time surface-layer decoupling over forest canopies in a land-surface model. *Bound.-Layer Meteor.*, **103**, 253–276, doi:10.1023/A:1017443021557.

Derbyshire, S. H., 1999a: Stable boundary layer modelling: Established approaches and beyond. *Bound.-Layer Meteor.*, **90**, 423–446, doi:10.1023/A:1001749007836.

——, 1999b: Boundary-layer decoupling over cold surfaces as a physical boundary instability. *Bound.-Layer Meteor.*, **90**, 297–325, doi:10.1023/A:1001710014316.

Donda, J. M. M., I. G. S. Van Hooijdonk, A. F. Moene, G. J. F. Van Heijst, H. J. H. Clercx, and B. J. H. Van de Wiel, 2015: Collapse of turbulence in a stably stratified channel flow: A transient phenomenon. *Quart. J. Roy. Meteor. Soc.*, **141**, 2137–2147, doi:10.1002/qj.2511.

——, ——, ——, ——, ——, and ——, 2016: The maximum sustainable heat flux in stably stratified channel flows. *Quart. J. Roy. Meteor. Soc.*, **142**, 781–792, doi:10.1002/qj.2680.

Duynkerke, P. G., 1999: Turbulence, radiation and fog in Dutch stable boundary layer. *Bound.-Layer Meteor.*, **90**, 447–477, doi:10.1023/A:1026441904734.

Edwards, J. M., 2009: Radiative processes in the stable boundary layer: Part II. The development of the nocturnal boundary layer. *Bound.-Layer Meteor.*, **131**, 127–146, doi:10.1007/s10546-009-9363-9.

England, D. E., and R. T. McNider, 1995: Stability functions based upon shear functions. *Bound.-Layer Meteor.*, **74**, 113–130, doi:10.1007/BF00715713.

Fernando, H. J. S., and J. C. Weil, 2010: Whither the stable boundary layer? *Bull. Amer. Meteor. Soc.*, **91**, 1475–1484, doi:10.1175/2010BAMS2770.1.

Flores, O., and J. J. Riley, 2011: Analysis of turbulence collapse in the stably stratified surface layer using direct numerical simulation. *Bound.-Layer Meteor.*, **139**, 241–259, doi:10.1007/s10546-011-9588-2.

Gallée, H., and Coauthors, 2015: Characterization of the boundary layer at Dome C (East Antarctica) during the OPALE summer campaign. *Atmos. Chem. Phys.*, **15**, 6225–6236, doi:10.5194/acp-15-6225-2015.

Genthon, C., M. S. Town, D. Six, V. Favier, S. Argentini, and A. Pellegrini, 2010: Meteorological atmospheric boundary layer measurements and ECMWF analyses during summer at Dome C, Antarctica. *J. Geophys. Res.*, **115**, D05104, doi:10.1029/2009JD012741.

——, D. Six, H. Gallée, P. Grigioni, and A. Pellegrini, 2013: Two years of atmospheric boundary layer observations on a 45-m tower at Dome C on the Antarctic plateau. *J. Geophys. Res. Atmos.*, **118**, 3218–3232, doi:10.1002/jgrd.50128.

Gibbs, J. A., E. Fedorovich, and A. Shapiro, 2015: Revisiting surface heat-flux and temperature boundary conditions in models of stably stratified boundary-layer flows. *Bound.-Layer Meteor.*, **154**, 171–187, doi:10.1007/s10546-014-9970-y.

Grachev, A., C. Fairall, P. Persson, E. Andreas, and P. Guest, 2005: Stable boundary-layer regimes: The SHEBA data. *Bound.-Layer Meteor.*, **116**, 201–235, doi:10.1007/s10546-004-2729-0.

Heusinkveld, B. G., A. F. G. Jacobs, A. A. M. Holtslag, and S. M. Berkowicz, 2004: Surface energy balance closure in an arid region: Role of soil and heat flux. *Agric. For. Meteor.*, **122**, 21–37, doi:10.1016/j.agrformet.2003.09.005.

Högström, U., 1996: Review of some basic characteristics of the atmospheric surface layer. *Bound.-Layer Meteor.*, **78**, 215–246, doi:10.1007/BF00120937.

Holdsworth, A. M., T. Rees, and A. H. Monahan, 2016: Parameterization sensitivity and instability characteristics of the maximum sustainable heat flux framework for predicting turbulent collapse. *J. Atmos. Sci.*, **73**, 3527–3540, doi:10.1175/JAS-D-16-0057.1.

Holtslag, A. A. M., and H. A. R. De Bruin, 1988: Applied modeling of the nighttime surface energy balance over land. *J. Appl. Meteor.*, **27**, 689–704, doi:10.1175/1520-0450(1988)027<0689:AMOTNS>2.0.CO;2.

——, G.-J. Steeneveld, and B. J. H. van de Wiel, 2007: Role of land-surface temperature feedback on model performance for the stable boundary layer. *Bound.-Layer Meteor.*, **125**, 361–376, doi:10.1007/s10546-007-9214-5.

——, and Coauthors, 2013: Stable atmospheric boundary layers and diurnal cycles: Challenges for weather and climate models. *Bull. Amer. Meteor. Soc.*, **94**, 1691–1706, doi:10.1175/BAMS-D-11-00187.1.

Huang, J., and E. Bou-Zeid, 2013: Turbulence and vertical fluxes in the stable atmospheric boundary layer. Part I: A large-eddy simulation study. *J. Atmos. Sci.*, **70**, 1513–1527, doi:10.1175/JAS-D-12-0167.1.

Lenderink, G., and A. A. M. Holtslag, 2004: An updated length-scale formulation for turbulent mixing in clear and cloudy boundary layers. *Quart. J. Roy. Meteor. Soc.*, **130**, 3405–3427, doi:10.1256/qj.03.117.

Louis, J.-F., 1979: A parametric model of vertical eddy fluxes in the atmosphere. *Bound.-Layer Meteor.*, **17**, 187–202, doi:10.1007/BF00117978.

Mackaro, S., R. McNider, and A. Pour-Biazar, 2012: Some physical and computational issues in land surface data assimilation of satellite skin temperatures. *Pure Appl. Geophys.*, **169**, 401–414, doi:10.1007/s00024-011-0377-0.

Mahrt, L., 2014: Stably stratified atmospheric boundary layers. *Annu. Rev. Fluid Mech.*, **46**, 23–45, doi:10.1146/annurev-fluid-010313-141354.

——, J. Sun, W. Blumen, T. Delany, and S. Oncley, 1998: Nocturnal boundary layer regimes. *Bound.-Layer Meteor.*, **88**, 255–278, doi:10.1023/A:1001171313493.

Malhi, Y. S., 1995: The significance of the dual solutions for heat fluxes measured by the temperature fluctuation method in stable conditions. *Bound.-Layer Meteor.*, **74**, 389–396, doi:10.1007/BF00712379.

McNider, R. T., D. E. England, M. J. Friedman, and X. Shi, 1995: Predictability of the stable atmospheric boundary layer. *J. Atmos. Sci.*, **52**, 1602–1614, doi:10.1175/1520-0469(1995)052<1602:POTSAB>2.0.CO;2.

——, and Coauthors, 2012: Response and sensitivity of the nocturnal boundary layer over land to added longwave radiative forcing. *J. Geophys. Res.*, **117**, D14106, doi:10.1029/2012JD017578.

Monahan, A. H., T. Rees, Y. He, and N. McFarlane, 2015: Multiple regimes of wind, stratification, and turbulence in the stable boundary layer. *J. Atmos. Sci.*, **72**, 3178–3198, doi:10.1175/JAS-D-14-0311.1.

Monteith, J. L., 1981: Evaporation and surface temperature. *Quart. J. Roy. Meteor. Soc.*, **107**, 1–27, doi:10.1002/qj.49710745102.

Morcrette, J.-J., 1991: Radiation and cloud radiation properties in the European Centre for Medium Range Weather Forecasts forecasting system. *J. Geophys. Res.*, **96**, 9121–9132, doi:10.1029/89JD01597.

Nieuwstadt, F. T. M., 2005: Direct numerical simulation of stable channel flow at large stability. *Bound.-Layer Meteor.*, **116**, 277–299, doi:10.1007/s10546-004-2818-0.

Poulos, G. S., and Coauthors, 2002: CASES-99: A comprehensive investigation of the stable nocturnal boundary layer. *Bull. Amer. Meteor. Soc.*, **83**, 555–581, doi:10.1175/1520-0477(2002)083<0555:CACIOT>2.3.CO;2.

Roman-Cascon, C., G. J. Steeneveld, C. Yague, M. Sastre, J. A. Arrillaga, and G. Maqueda, 2016: Forecasting radiation fog at climatologically contrasting sites: Evaluation of statistical methods and WRF. *Quart. J. Roy. Meteor. Soc.*, **142**, 1048–1063, doi:10.1002/qj.2708.

Shi, X., R. T. McNider, D. E. England, M. J. Friedman, W. Lapenta, and W. B. Norris, 2005: On the behavior of the stable boundary layer and role of initial conditions. *Pure Appl. Geophys.*, **162**, 1811–1829, doi:10.1007/s00024-005-2694-7.

Sorbjan, Z., 2006: Local structure of turbulence in stably stratified boundary layers. *J. Atmos. Sci.*, **63**, 1526–1537, doi:10.1175/JAS3704.1.

Steeneveld, G. J., B. J. H. van de Wiel, and A. A. M. Holtslag, 2006: Modeling the evolution of the atmospheric boundary layer coupled to the land surface for three contrasting nights in CASES-99. *J. Atmos. Sci.*, **63**, 920–935, doi:10.1175/JAS3654.1.

Stolaki, S., I. Pytharoulis, and T. Karacostas, 2012: A study of fog characteristics using a coupled WRF–COBEL model over Thessaloniki Airport, Greece. *Pure Appl. Geophys.*, **169**, 961–981, doi:10.1007/s00024-011-0393-0.

Sullivan, P. P., J. C. Weil, E. G. Patton, H. J. H. Jonker, and D. Mironov, 2016: Turbulent winds and temperature fronts in large-eddy simulations of the stable atmospheric boundary layer. *J. Atmos. Sci.*, **73**, 1815–1840, doi:10.1175/JAS-D-15-0339.1.

Sun, J., L. Mahrt, R. Banta, and Y. Pichugina, 2012: Turbulence regimes and turbulence intermittency in the stable boundary layer during CASES-99. *J. Atmos. Sci.*, **69**, 338–351, doi:10.1175/JAS-D-11-082.1.

Taylor, P. A., 1971: A note on the log-linear velocity profile in stable conditions. *Quart. J. Roy. Meteor. Soc.*, **97**, 326–329, doi:10.1002/qj.49709741308.

Thorpe, A. J., and T. H. Guymer, 1977: The nocturnal jet. *Quart. J. Roy. Meteor. Soc.*, **103**, 633–653, doi:10.1002/qj.49710343809.

Van de Wiel, B. J. H., A. F. Moene, G. J. Steeneveld, O. K. Hartogensis, and A. A. M. Holtslag, 2007: Predicting the collapse of turbulence in stably stratified boundary layers. *Flow, Turbul. Combust.*, **79**, 251–274, doi:10.1007/s10494-007-9094-2.

——, ——, H. J. J. Jonker, P. Baas, S. Basu, J. M. M. Donda, J. Sun, and A. A. M. Holtslag, 2012a: The minimum wind speed for sustainable turbulence in the nocturnal boundary layer. *J. Atmos. Sci.*, **69**, 3116–3127, doi:10.1175/JAS-D-12-0107.1.

——, ——, and ——, 2012b: The cessation of continuous turbulence as precursor of the very stable nocturnal boundary layer. *J. Atmos. Sci.*, **69**, 3097–3115, doi:10.1175/JAS-D-12-064.1.

Van Hooijdonk, I. G. S., J. J. M. Donda, F. C. Bosveld, and B. J. H. Van de Wiel, 2015: Shear capacity as prognostic for nocturnal boundary layer regimes. *J. Atmos. Sci.*, **72**, 1518–1532, doi:10.1175/JAS-D-14-0140.1.

——, A. F. Moene, M. Scheffer, H. J. H. Clercx, and B. J. H. Van de Wiel, 2017: Early warning signals for regime transition in the stable boundary layer: A model study. *Bound.-Layer Meteor.*, **162**, 283–306, doi:10.1007/s10546-016-0199-9.

Vignon, E., C. Genthon, H. Barral, C. Amory, G. Picard, H. Gallée, G. Casasanta, and S. Argentini, 2017a: Momentum- and heat-flux parametrization at Dome C, Antarctica: A sensitivity study. *Bound.-Layer Meteor.*, **162**, 341–367, doi:10.1007/s10546-016-0192-3.

——, and Coauthors, 2017b: Stable boundary layer regimes at Dome C: Antarctica. *Quart. J. Roy. Meteor. Soc.*, doi:10.1002/qj.2998, in press.

Vose, R. S., D. R. Easterling, and B. Gleason, 2005: Maximum and minimum temperature trends for the globe: An update through 2004. *Geophys. Res. Lett.*, **32**, L23822, doi:10.1029/2005GL024379.

Walters, J. T., R. T. McNider, X. Shi, and W. B. Norris, 2007: Positive surface temperature feedback in the stable nocturnal boundary layer. *Geophys. Res. Lett.*, **34**, L12709, doi:10.1029/2007GL029505.

Wieringa, J., 1989: Shapes of annual frequency distributions of wind speed observed on high meteorological masts. *Bound.-Layer Meteor.*, **47**, 85–110, doi:10.1007/BF00122324.

Wyngaard, J. C., 2010: *Turbulence in the Atmosphere.* Cambridge University Press, 393 pp.

Zilitinkevich, S. S., T. Elperin, N. Kleeorin, I. Rogachevskii, I. Esau, T. Mauritsen, and M. W. Miles, 2008: Turbulent energetics in stably stratified geophysical flows: Strong and weak mixing regimes. *Quart. J. Roy. Meteor. Soc.*, **134**, 793–799, doi:10.1002/qj.264.